

Top-down beta enhances bottom-up gamma.

Abbreviated title: Top-down beta enhances bottom-up gamma.

Craig G. Richter^{1,*}, William H. Thompson^{1,2,*}, Conrado A. Bosman^{3,4} Pascal Fries^{1,3}

¹ Ernst Strüngmann Institute (ESI) for Neuroscience in Cooperation with Max Planck Society, Deutschordenstraße 46, 60528 Frankfurt, Germany

² Department of Clinical Neuroscience, Karolinska Institute, Nobels Väg 9, 171 77 Solna, Sweden

³ Donders Institute for Brain, Cognition and Behaviour, Kapittelweg 29, Radboud University, 6525 EN Nijmegen, Netherlands

⁴ Swammerdam Institute for Life Sciences, Center for Neuroscience, Faculty of Science, University of Amsterdam, Sciencepark 904, 1098 XH Amsterdam, Netherlands

*C.R. and W.T. contributed equally to this study

Correspondence should be addressed to Dr. Craig Richter or Dr. Pascal Fries, Ernst Strüngmann Institute (ESI) for Neuroscience in Cooperation with Max Planck Society, Deutschordenstraße 46, 60528 Frankfurt, Germany. E-mails: craig.richter@esi-frankfurt.de, pascal.fries@esi-frankfurt.de.

Pages: 31

Figures: 8

Number of words: Abstract: 127; Introduction: 406; Discussion: 1334

Conflict of Interest: The authors declare no competing financial interests.

Acknowledgements: This work was supported by DFG (SPP 1665, FOR 1847, FR2557/5-1-CORNET), EU (HEALTH-F2-2008-200728-BrainSynch, FP7-604102-HBP), a European Young Investigator Award, National Institutes of Health (1U54MH091657-WU-Minn-Consortium-HCP), the LOEWE program (NeFF) and the FLAG-ERA JTC 2015 project CANON (co-funded by NWO to CAB). We would like to thank Julien Vezoli for his assistance in ROI definition, co-registration and construction of anatomical renderings.

1 Abstract

2 Several recent studies have demonstrated that the bottom-up signaling of a visual stimulus is
3 subserved by interareal gamma-band synchronization, whereas top-down influences are mediated by
4 alpha-beta band synchronization. These processes may implement top-down control of stimulus
5 processing if top-down and bottom-up mediating rhythms are coupled via cross-frequency interaction.
6 To test this possibility, we investigated Granger-causal influences among awake male macaque
7 primary visual area V1, higher visual area V4 and parietal control area 7a during attentional task
8 performance. Top-down 7a-to-V1 beta-band influences enhanced visually driven V1-to-V4 gamma-
9 band influences. This enhancement was spatially specific and largest when beta-band activity
10 preceded gamma-band activity by ~ 0.1 s, suggesting a causal effect of top-down processes on
11 bottom-up processes. We propose that this cross-frequency interaction mechanistically subserves the
12 attentional control of stimulus selection.

13 Significance Statement

14 Contemporary research indicates that the alpha-beta frequency band underlies top-down control,
15 while the gamma-band mediates bottom-up stimulus processing. This arrangement inspires an
16 attractive hypothesis, which posits that top-down beta-band influences directly modulate bottom-up
17 gamma band influences via cross-frequency interaction. We evaluate this hypothesis determining that
18 beta-band top-down influences from parietal area 7a to visual area V1 are correlated with bottom-up
19 gamma frequency oscillations from V1 to area V4, in a spatially specific manner, and that this
20 correlation is maximal when top-down activity precedes bottom-up activity. These results show that for
21 top-down processes such as spatial attention, elevated top-down beta-band influences directly
22 enhance feedforward stimulus induced gamma-band processing, leading to enhancement of the
23 selected stimulus.

24 Introduction

25 Many cognitive effects in vision can only be explained by invoking the concept of top-down influences
26 (Gilbert and Sigman, 2007). For example, when top-down influences pre-allocate attention to specific
27 spatial locations, stimulus processing is more accurate and/or faster. Correspondingly, neurons in
28 higher visual areas show enhanced firing when processing attended stimuli. These neurophysiological
29 consequences of top-down control must be mediated by corresponding anatomical projections.
30 Indeed, anatomical studies have documented projections in the top-down direction that are as
31 numerous as bottom-up projections. Bottom-up and top-down projections show different characteristic
32 laminar patterns of origin and termination, and the pattern of interareal pairwise projections abides by
33 a global hierarchy (Felleman and Van Essen, 1991; Hilgetag et al., 1996; Markov et al., 2014).
34 Recently, it has been shown in both macaque and human visual cortex, that the pattern of anatomical
35 projections is closely correlated to a pattern of frequency-specific directed interareal influences.
36 Influences mediated by bottom-up projections are primarily carried by gamma-band synchronization;
37 influences mediated by top-down projections are primarily carried by alpha-beta-band synchronization
38 (Bastos et al., 2012; Bosman et al., 2012; Grothe et al., 2012; Jia et al., 2013; van Kerkoerle et al.,
39 2014; Bastos et al., 2015b; 2015c; Michalareas et al., 2016). A similar association of higher frequency
40 bands with bottom-up and lower frequency bands with top-down signaling has also been found in
41 other systems (Colgin et al., 2009; Bieri et al., 2014; Fontolan et al., 2014) and related to respective
42 task demands (von Stein and Sarnthein, 2000; Buschman and Miller, 2007).

43 Here, we investigate directly whether top-down influences actually modulate bottom-up influences. We
44 simultaneously assess influences in both directions through multi-area electrophysiology and
45 frequency-resolved Granger causality analysis. We find that on an epoch-by-epoch basis, top-down
46 beta-band influences enhance bottom-up gamma-band influences. This effect is spatially specific, i.e.
47 bottom-up gamma-band influences depend most strongly on the top-down beta-band influences that
48 are directed to the origin of the bottom-up influence. Spontaneous enhancements in top-down beta-
49 band influences are followed ~ 0.1 s later by enhancements in bottom-up gamma-band influences,
50 suggestive of a causal relation.

51 We suggest that this is a mechanism for the implementation of spatially selective attention. Attentional
52 control areas in posterior parietal cortex contain maps of visual space, with neuronal ensemble activity

53 describing the spatial location of a subject's attention (Bisley and Goldberg, 2003). These neurons
54 likely exert top-down beta-band influences on retinotopically corresponding parts of early visual cortex,
55 which in turn enhance the bottom-up forwarding of visual stimuli.

56 Materials and Methods

57 *Visual stimulation and behavioral task.* The experiment was approved by the ethics committee of the
58 Radboud University Nijmegen (Nijmegen, The Netherlands). Two adult male macaque monkeys
59 (monkey K and monkey P, both macaca mulatta) were used in this study. During experiments,
60 monkeys were placed in a dimly lit booth facing a CRT monitor (120 Hz non-interlaced). When they
61 touched a bar, a fixation point was presented, and gaze had to remain within the fixation window
62 throughout the trial (monkey K: 0.85 deg radius, monkey P: 1 deg radius), otherwise the trial would be
63 terminated and a new trial would commence. Once central fixation had been achieved and a
64 subsequent 0.8 s pre-stimulus interval had elapsed, two isoluminant and isoeccentric drifting
65 sinusoidal gratings were presented, one in each visual hemifield (diameter: 3 deg, spatial frequency:
66 ≈ 1 cycle/deg, drift velocity: ≈ 1 deg/s, resulting temporal frequency: ≈ 1 cycle/s, contrast: 100%). Blue
67 and yellow tints were randomly assigned to each of the gratings on each trial (Fig. 1A). Following a
68 random delay interval (monkey K : 1 - 1.5 s; monkey P : 0.8 - 1.3 s), the central fixation point changed
69 color to match one of the drifting gratings, indicating that this grating was the target stimulus, i.e. the
70 fixation point color was the attentional cue. When the target stimulus was positioned in the visual
71 hemifield contralateral to the recorded hemisphere, we refer to this condition as attend-contra,
72 whereas when the target was in the ipsilateral hemifield with respect to the ECoG grid, this condition is
73 labeled attend-ipsi. Either the target or distracter stimulus could undergo a subtle change in shape
74 consisting of a transient bending of the bars of the grating (0.15 s duration of the full bending cycle).
75 This change could occur at any monitor refresh from 0.75 s to 5 s (monkey K), and 4 s (monkey P)
76 after stimulus onset. Bar releases within 0.15 - 0.5 s after target changes were rewarded. If stimulus
77 changes occurred before the cue indicated which stimulus was the target, reports were rewarded in a
78 random half of trials. Bar releases after distracter changes terminated the trial without reward. Trials
79 were pooled from both contra and ipsi conditions, except where explicit comparisons of these
80 conditions were made.

81 *Neurophysiological recordings and signal preprocessing.* LFP recordings were made via a 252
82 channel electrocorticographic grid (ECoG) implanted subdurally over the left hemisphere (Rubehn et
83 al., 2009). Data from the same animals, partly overlapping with the data used here, have been used in
84 several previous studies (Bosman et al., 2012; Pinotsis et al., 2014; Brunet et al., 2014a; 2014b; 2015;
85 Richter et al., 2015; Vinck et al., 2015; Bastos et al., 2015b; 2015c; Lewis et al., 2016). Recordings
86 were sampled at approximately 32 kHz with a passband of 0.159 – 8000 Hz using a Neuralynx Digital
87 Lynx system. The raw recordings were low-pass filtered at 250 Hz, and downsampled to 1 kHz. The
88 electrodes were distributed over eight 32-channel headstages, and referenced against a silver wire
89 implanted onto the dura overlying the opposite hemisphere. The electrodes were re-referenced via a
90 bipolar scheme to achieve 1) greater signal localization 2) cancellation of the common reference,
91 which could corrupt the validity of connectivity metrics, 3) to reject headstage specific noise. The
92 bipolar derivation scheme subtracted the recordings from neighboring electrodes (spaced 2.5 mm)
93 that shared a headstage, resulting in 218 bipolar derivations, henceforth referred to as “sites” (see
94 Bastos et al. (2015c) for a detailed description of the re-referencing procedure). The site locations are
95 shown as spheres in Figure 1b (monkey K: light gray, monkey P: black).

96 All signal processing was conducted in MATLAB (MathWorks, USA) and using the FieldTrip toolbox
97 (<http://www.fieldtriptoolbox.org/>) (Oostenveld et al., 2011). Raw data were cleaned of line noise via the
98 subtraction of 50, 100, and 150 Hz components fit to the data using a discrete Fourier transform.
99 Following trial epoching (see below for details), epochs for each site were de-meanned by subtracting
100 the mean over all time points in the epoch. Epochs exceeding 5 standard deviations of all data from
101 the same site in the same session were rejected. In addition, epochs were manually inspected and
102 epochs with artifacts were rejected. The remaining epochs were normalized by the standard deviation
103 across all data in all epochs from the same site in the same recording session. Subsequently, all
104 epochs of a given site were combined across sessions.

105 *Region of interest definition.* Three regions-of-interest (ROIs) were selected for the current study: V1,
106 V4, and area 7A (referred to simply as “7A”). ROIs were defined based on comparison of the electrode
107 locations (co-registered to each monkey’s anatomical MRI and warped to the F99 template brain in
108 CARET (Van Essen, 2012), with multiple cortical atlases of the macaque (see Bastos et al. (2015c) for
109 a detailed description). Recording sites composing each ROI were co-registered to a common

110 template (INIA19, (Rohlfing et al., 2012)), as were the Paxinos ROI definitions (Paxinos et al., 1999).
111 The V1/V2 combined definition of Paxinos et al. (1999), is shown in Figures 1B, 3G (red) for simplicity
112 due to uncertainty across atlases of the V1/V2 border. Recording site selection was based on multiple
113 atlases with no recording sites selected that were believed to belong to area V2. Based on these ROI
114 definitions, 77 recording sites were selected from area V1 (monkey K: 29, monkey P: 48), 31 from
115 area V4 (monkey K: 17, monkey P: 14), and 18 from area 7A (monkey K: 8, monkey P: 10).

116 *Segmenting data into periods and epochs.* Each successfully completed trial contained three periods:
117 The fixation, the stimulation and the attention period. The fixation period was the time between fixation
118 onset and stimulus onset. During the fixation period, monkeys fixated on a fixation point on a gray
119 screen, and there was no stimulus presented and no cue had been nor was presented during that
120 time. The stimulation period was the time between onset of the stimuli and either a change in one of
121 the stimuli or cue onset. During the stimulation period, monkeys kept fixation, the stimuli were
122 continuously present, one tinted yellow the other blue, chosen randomly, and the fixation point had not
123 yet assumed a color, and thereby the attentional cue had not been given. The attention period was the
124 time between cue onset and a target or distracter change, whichever occurred first. During the
125 attention period, monkeys kept fixation, the stimuli were continuously present with their tints, and the
126 fixation point was tinted in one of these colors, thereby providing the attentional cue.

127 The fixation, stimulation and attention periods all were of variable lengths across trials. The spectral
128 analysis was based on epochs of fixed lengths. Therefore, the task periods were cut into epochs.
129 Longer trials contributed correspondingly more epochs. We aimed at excluding data soon after events,
130 like stimulus onset and cue onset, to minimize effects of post-event transients and non-stationarities
131 on the metrics of rhythmicity and synchronization. Therefore, from the fixation period, we used the last
132 0.5 s before stimulus onset; from the stimulation period, the first 0.3 s after stimulus onset were
133 discarded; for the attention period, the first 0.3 s after cue onset were discarded.

134 For the analyses of Figure 2 and Figure 3, the remaining parts of the described periods were
135 segmented into 0.5 s epochs with 60% overlap. This overlap allows for the application of Welch's
136 method (Welch, 1967) and was selected as an optimal overlap for the multitaper method, while
137 maintaining a reasonable computational load (Thomson, 1977; Percival and Walden, 1993). This
138 resulted in 6822 fixation epochs (Monkey K: 3384, Monkey P: 3438), 13675 stimulation epochs

139 (Monkey K: 8109, Monkey P: 5566), and a total of 16212 attend epochs (Monkey K: 7275, Monkey P:
140 8937), of which 8313 were attend-contralateral epochs (Monkey K: 3819, Monkey P: 4494) and 7899 were
141 attend-ipsilateral epochs (Monkey K: 3456, Monkey P: 4443).

142 For the analyses of Figures 4-7, the same procedure was followed, but using only the attention period
143 and segmenting it into epochs without overlap, because the correlation analyses shown in these
144 figures require independent epochs. This resulted in fewer epochs, totaling 6414 attend epochs
145 (Monkey K: 2655, Monkey P: 3759).

146 For the analyses of Figure 8, the attention period was segmented into many overlapping 0.5 s epochs,
147 with epochs centers stepped by 0.005 s and epochs fully contained within 0.3-2 s after cue onset. This
148 was done, because the analysis required GC influence time series. It resulted in a total of 878 time
149 series (Monkey K: 398, Monkey P: 480).

150 *Spectral Analysis of power, phase locking and directed influences.* The 0.5 s epochs were tapered and
151 Fourier transformed using the Fast Fourier Transform (FFT). For frequencies from 0-50 Hz, a Hann
152 taper was utilized, whereas for frequencies above 50 Hz, the multitaper method (MTM) was used to
153 improve the spectral concentration of the gamma rhythm (Thomson, 1982; Percival and Walden,
154 1993). We applied 5 tapers, resulting in a spectral smoothing of +/- 6 Hz. All epochs were zero-padded
155 to 1 s, resulting in a spectral resolution of 1 Hz. The coefficients resulting from the FFT were used to
156 determine power-spectral densities (PSDs) and cross-spectral densities (CSDs), which are the basis
157 for the two employed connectivity metrics: pairwise phase consistency (PPC) (Vinck et al., 2010), and
158 Granger causality (GC) (Granger, 1969; Bressler and Seth, 2011). For the display of power spectra,
159 the power dropoff with frequency, often referred to as $1/f$, was partly compensated by multiplying
160 power values at each frequency by the respective frequency values; for example, the power at 40 Hz
161 was multiplied by 40 (Sirota et al., 2008) (Fig. 2A-F). The PPC metric (Fig. 2G-J, Fig. 3A, B), in
162 contrast to the classic coherence metric, does not contain a sample-size bias, that is, it can be directly
163 compared between different numbers of epochs. The GC metric (Fig. 3C-F) was computed directly
164 from the CSDs, using non-parametric spectral matrix factorization, in contrast to the traditional
165 parametric method based on autoregressive modeling (Dhamala et al., 2008). Connectivity metrics
166 were computed for all interareal site pairs of the ROI pairs V1-V4 and V1-7A.

167 *Statistical comparison of spectral metrics.* Statistical comparison of interaction metrics between
168 conditions used non-parametric randomization, entailing correction for multiple comparisons across
169 frequencies (Maris and Oostenveld, 2007). We illustrate this for PPC. The observed PPC spectra
170 (without randomization) are derived by 1) Calculating PPC spectra across all epochs of a given
171 condition in a given animal, separately for all site pairs of the relevant ROI pair, 2) Averaging PPC
172 spectra across those site pairs, 3) Averaging across the two animals after aligning the peaks of the
173 respective frequency bands. We performed 1000 randomizations, each constituting the null
174 hypothesis. For each randomization, the following steps were performed: 1) Epochs were randomly
175 distributed between conditions. 2) The same steps as for the observed PPC spectra were followed.
176 3) The maximal absolute difference value across all frequencies was retained and placed into the
177 randomization distribution. The observed differences were compared against the distribution of
178 maximal absolute differences. Observed absolute difference values greater than the 97.5th percentile
179 of the randomization distribution were considered significant at $p < 0.05$. The selection of the maximal
180 absolute difference value per randomization implements the correction for multiple comparisons
181 across frequencies (Nichols and Holmes, 2002). This procedure was used for both PPC and
182 GC influences spectra, separately for the respective frequency bands, either comparing stimulation to
183 fixation or attend-*contra* to attend-*ipsi*.

184 The GC influence metric is known to be biased by sample size (Bastos and Schoffelen, 2015a), thus
185 the number of epochs per attention condition needed to be balanced for each monkey. This was
186 accomplished by finding the condition with the fewest epochs, and randomly selecting this number of
187 epochs from the other condition.

188 The comparison of top-down versus bottom-up GC was performed on the pooled data from the attend-
189 *contra* and attend-*ipsi* conditions. Since this was a within-condition comparison, no balancing of epoch
190 numbers was needed, and all epochs from both attention conditions were used. The statistical
191 analysis of the difference between top-down and bottom-up GC could not be obtained using a non-
192 parametric randomization framework, because top-down and bottom-up GC are not properties of
193 specific sets of epochs, but rather are expressed by all trials simultaneously. Therefore, an alternative
194 statistical approach was used, namely the bootstrap (Efron and Tibshirani, 1994). Like with the
195 randomization approach, the statistic of interest (in this case the top-down/bottom-up GC difference) is

196 recomputed on each bootstrap resample, giving rise to a distribution of surrogate values. Following
197 Efron and Tibshirani (1994), a confidence interval was constructed from the surrogate distribution. To
198 assess the statistical significance at $p < 0.05$ (two-tailed), we find the 2.5th and 97.5th percentile values
199 from the surrogate distribution of differences between top-down and bottom-up GC. This naturally
200 forms the 95% confidence interval such that if zero lies outside of this interval, we may conclude that
201 the result is significant at a level of $p < 0.05$. This method does not control for multiple comparisons, but
202 it can be easily modified to do so using the same logic as employed by Maris and Oostenveld (2007).
203 We performed 1000 bootstrap resamples. For each resample we determined the absolute difference
204 across frequencies between the bootstrap resample spectrum and the average of all bootstrap
205 resamples, and retained the maximum of this value across frequencies. Thus, we are guaranteed to
206 form the largest confidence interval possible across frequencies and in so doing construct an omnibus
207 confidence interval that controls for the multiple comparisons. This confidence interval is applied to
208 each frequency, and where it does not contain zero, the result is significant at $p < 0.05$. To conduct
209 group level statistics, the omnibus statistic is derived from the mean of each bootstrap resample of the
210 difference between top-down and bottom-up spectra across both monkeys (first averaged within-
211 subject across pairs), such that the mean of the empirical difference across the monkeys can be
212 assessed for significance.

213 *Median split analysis.* For the median split analysis, we used a jackknife approach, which leaves out
214 one epoch at a time. The remaining epochs form a jackknife replication (JR). There are as many JRs
215 as there are epochs. 7A-to-V1 beta-band GC (beta peak ± 1 Hz) was computed for all JRs. The
216 resulting values were median split, and V1-to-V4 GC computed for the corresponding sets of epochs.
217 The jackknife procedure inverts the distribution of single-epoch GC values (Richter et al., 2015), such
218 that the upper half of JR values corresponds to the lower half of the true single epoch values. The
219 observed differences in V1-to-V4 GC were tested for significance as described for the spectral
220 metrics, using 200 randomizations. The analysis always included a 7A-to-V1 site pair and a V1-to-V4
221 site pair, sharing the same V1 site. We refer to this configuration as a triplet, or sometimes as
222 7A-to-V1-to-V4 triplet. There was a total of 10664 triplets (Monkey K: 3944, Monkey P=6720). The
223 median split analysis is presented in three forms: 1) for an example triplet, 2) for all triplets, followed
224 by averaging of V1-to-V4 GC, 3) for median splits based on the averaged 7A-to-V1 GC, followed by

225 averaging of V1-to-V4 GC. For approaches 2) and 3), individual peak frequencies were aligned across
226 monkeys. The median split analysis was repeated for the inverse direction, splitting epochs based on
227 V1-to-V4 gamma-band GC jackknife replications (average of the peak \pm 5 Hz), followed by averaging
228 of 7A-to-V1 GC.

229 *Binning of sorted trials.* To determine correlation values after sorting and binning the data, JR values
230 of 7A-to-V1 beta-band GC were sorted and binned into either 5, 10, 50, or 100 bins of equal size. Per
231 bin, JR values of 7A-to-V1 beta-band GC and of V1-to-V4 gamma GC were averaged. The Spearman
232 rank correlation was determined across bins. When data were combined across monkeys, correlation
233 coefficients were averaged across triplets for each monkey, and then averaged across monkeys.
234 Statistical testing was based on permutations of bin order. Per permutation, bin order was
235 randomized, and correlation coefficients were computed and averaged as for the observed data. This
236 was applied 10000 times, resulting in minimal p-values of 0.0001.

237 *Jackknife Correlation.* We aimed at quantifying the correlation between epoch-by-epoch fluctuations in
238 two GC influences. This is normally precluded by the fact that GC influences are not defined per single
239 data epoch (without substantially sacrificing spectral resolution and/or signal-to-noise ratio). Therefore,
240 we used the Jackknife Correlation (JC), which quantifies the correlation by first calculating GC
241 influences for all leave-one-out subsamples (i.e. the jackknife replications of all epochs) and then
242 correlating these values (Richter et al., 2015). For each leave-one-out subsample, the GC or any other
243 smooth function F of the data can be defined as follows:

244

$$F_{x_j} = F(x_1, x_2, \dots, x_{j-1}, x_{j+1}, \dots, x_n) \quad (1)$$

245

246 , where x specifies the pair of recording sites and j specifies the index of the left-out observation, here
247 the epoch. Attend contra and attend ipsi conditions were combined for the JC analysis. The JC is
248 defined using the following formula:

249

$$JC_{F_x F_y} = \frac{1}{n-1} \sum_{j=1}^n \left(\frac{F_{x_j} - \bar{F}_x}{s_{F_x}} \right) \left(\frac{F_{y_j} - \bar{F}_y}{s_{F_y}} \right) \quad (2)$$

250

251 , where n is defined as the number of jackknife replications and is equal to the total number of epochs,
252 F_{x_j} and F_{y_j} are the jackknife replications, \bar{F}_x and \bar{F}_y are the means of the jackknife replications, and s_{F_x}
253 and s_{F_y} are the standard deviations of the jackknife replications. To use the JC with the Spearman
254 correlation metric, we applied the above formula on the ranks of F_{x_j} and F_{y_j} .

255 For the statistical analysis of the observed JC values, we created a distribution of 1000 JC values
256 under a realization of the null hypothesis of independence between the 7A-to-V1 and V1-to-V4 GC
257 components of each triplet. This was realized by calculating JC between randomly permuted orderings
258 of jackknife replications of 7A-to-V1 and V1-to-V4 GC influences, which is equivalent to calculating the
259 JC between GC influences after leaving out a random epoch for the 7A-to-V1 GC and a random epoch
260 for the V1-to-V4 GC influence without replacement. To control for multiple comparisons across the
261 frequency-frequency combinations, the max-based approach (see above) was again employed. For
262 each permutation, the maximum absolute Spearman's rho value was selected, giving rise to an
263 omnibus distribution of surrogate correlation coefficients. For the example triplet, the observed values
264 were compared to the distribution of maximum absolute surrogate correlation values. For the average
265 across triplets, the average was first calculated over triplets, then over monkeys, after aligning to their
266 respective peak frequencies. For statistical testing, the same randomization was applied to all triplets
267 of a given monkey, subsequent averaging was performed as for the observed data, and the maximum-
268 based multiple comparison correction was applied as for the example triplet. An additional JC analysis
269 first averaged all 7A-to-V1 site pairs and all V1-to-V4 site pairs to form one triplet per monkey. JC
270 values were then averaged over monkeys. For statistical testing, the randomization was applied to this
271 triplet per monkey, followed by averaging over monkeys, and the max-based multiple comparison
272 correction.

273 For testing spatial specificity, we analyzed recording site triplets, which did not share the same V1 site
274 (see Results for additional details): 7A-to-V1_aV1_b-to-V4. Since a vast number of such triplets exist, yet
275 we wished to select a number equal to the original number of triplets to control potential statistical

276 bias, we randomly selected a number of 7A-to-V1_aV1_b-to-V4 triplets that matched the original number
277 of 7A-to-V1-to-V4 triplets evaluated for each monkey. We repeated this procedure 100 times and
278 averaged the outcomes. Results were plotted against the average distance between the two V1 sites,
279 V1_a and V1_b, obtained for each distance interval.

280 *Weighted Jackknife Correlation.* JCs might be particularly strong for triplets with strong 7A-to-V1 beta-
281 band GC and/or strong V1-to-V4 gamma-band GC. To test for this, we weighted JC by multiplying it
282 with the product of the 7A-to-V1 beta and the V1-to-V4 gamma GC magnitudes. Weights were
283 normalized such that the average weight across triplets was one. The weighted and the unweighted
284 JC values were separately averaged per monkey and then across monkeys. Statistics were based on
285 random exchanges between weighted and unweighted values, within each monkey, and subsequent
286 averaging as for the observed data. Randomization was applied 1000 times.

287 *Lagged Jackknife Correlation (LJC).* We were interested in whether the correlation between top-down
288 beta GC and bottom-up gamma GC depended on their time lag. We started out by using the JC as
289 described above. To smooth the results against shifts in peak frequencies over time, we used the
290 average of the range of the top-down beta GC peak ± 5 Hz, and the bottom-up gamma GC peak ± 10
291 Hz. Since a given jackknife replication eliminated the same epoch for the calculation of both GC
292 influences, this established the correlation at zero time-lag. To investigate the dependence of JC on
293 time lag between GCs, we computed the JC between GC influences calculated from epochs that were
294 offset by a variable lag. The epochs were stepped at intervals of $t=0.005$ s. The offsets were stepped
295 at $\tau=0.005$ s. Note that stepping of intervals and offsets was in principle independent and could have
296 been different, but it was chosen to be identical to speed up computation. We refer to this as lagged
297 JC (LJC):

298

$$LJC_{F_x F_y}(\tau, t) = \frac{1}{n-1} \sum_{j=1}^n \left(\frac{F_{x_j,t} - \bar{F}_x}{S_{F_x t}} \right) \left(\frac{F_{y_j,t+\tau} - \bar{F}_y}{S_{F_y t+\tau}} \right) \quad (3)$$

299

300 τ was chosen to cover a range of lags from -0.5 s to 0.5 s. The GC calculation itself was as in the
301 previous zero-lag JC, using 0.5 s and the tapering specified above. LJC was calculated across trials,

302 i.e. leaving out an entire trial at a time (this is different from the previous zero-lag JC, which used
303 multiple non-overlapping epochs per trial if available). The data that was available per trial allowed for
304 multiple realizations of the two epochs with a particular lag. For each lag, LJC was calculated
305 separately for all possible realizations and averaged. The number of possible realizations decreases
306 as the lag between top-down beta GC and bottom-up gamma GC increases, resulting in fewer LJC
307 computations that are averaged. This results in a noisier estimate at larger lags, but no systematic
308 bias in the average JC value. The number of epochs that each LJC is computed upon always equals
309 the number of trials. Formally, this implementation of the LJC is defined as:

310

$$LJC_{F_x F_y}(\tau) = \frac{1}{m - \tau} \sum_{t=1}^{m-\tau} \left[\frac{1}{n-1} \sum_{j=1}^n \left(\frac{F_{x_{j,t}} - \bar{F}_{x_t}}{S_{F_{x_t}}} \right) \left(\frac{F_{y_{j,t+\tau}} - \bar{F}_{y_{t+\tau}}}{S_{F_{y_{t+\tau}}}} \right) \right] \quad (4)$$

311

312 , where m is the number of 0.5 s windows, stepped at 0.005 s, that fit into the trial length of 1.7 s.

313 Statistical significance was assessed using the same logic as used for the JC, where the epoch order
314 of one member of the JC was permuted with respect to the other. For the LJC, the permutation was
315 identical for each time step and lag, to be conservative. Multiple comparison correction must take
316 place over the multiple lags, which was achieved by taking the maximum absolute Spearman's rho
317 value across lags for each permutation. The resulting distribution was used to assess the probability
318 that the observed result at each lag occurred by chance. The observed and the permutation metrics
319 were first averaged over all triplets per monkey and then averaged over the two monkeys, to give
320 equal weight to both subjects.

321 We wished to assess whether the LJC peak lag of -0.105 s was significantly different from a lag of
322 zero. We did so using a jackknife method to determine the standard error of the peak position in
323 milliseconds (Efron, 1981). In this case, we leave out a specific triplet to assess the variability of the
324 peak. The jackknife procedure causes a compression of the variance (Richter et al., 2015), thus the
325 0.005 s sampling grid would not be sufficient to represent the peak positions of the jackknife
326 replications. To account for this, we cubic-spline interpolated each replication to a resolution of 1e-6 s,
327 which proved adequate to represent the variance of the peak. The peak of each jackknife replication

13

328 was found using a Gaussian fit of the smoothed correlation as a function of lag (findpeaksG.m by T.C
329 O'Haver). We then derived the standard error of the estimator, and converted this to a t-score by
330 dividing the mean peak lag value of the jackknife replications by the estimated standard error. The
331 significance of this t-value was then assessed against Student's t-distribution. At the group level, this
332 procedure entails concatenating the data from both monkeys, and leaving out each triplet once. Based
333 on this group estimate of the standard error, a t-value is derived, as above, and assessed for statistical
334 significance.

335 Results

336 Top-Down Versus Bottom-Up Spectral Asymmetries and their Stimulus and Task 337 Dependence

338 We performed electrocorticographic (ECoG) recordings from large parts of the left hemisphere in two
339 macaque monkeys performing a selective attention task (Fig. 1). From the ECoG recording sites, we
340 selected three ROIs (Fig. 1B), according to the following criteria: 1) One ROI should be a high-level
341 control area, one ROI a low-level visual area, and one ROI a higher-level visual area; 2) ECoG
342 coverage should be as good as possible; 3) ROIs should not be directly abutting, to avoid ambiguity in
343 boundary definition and to minimize volume conduction. These criteria led to the selection of areas 7A,
344 V1 and V4. The ROI pair 7A-V1 constitutes a clear top-down pathway with documented projections
345 from a very high-level control area to primary visual cortex (Markov et al., 2014; Bastos et al., 2015c;
346 Michalareas et al., 2016). The ROI pair V1-V4 constitutes a clear bottom-up pathway emerging from
347 V1, i.e. the area targeted by the top-down 7A-to-V1 influence. For both ROI pairs, the ECoG provided
348 good coverage. The central aim was to determine whether the top-down influence was modulating the
349 bottom-up influence.

350 To assess the individual frequency bands for each monkey (monkey K and monkey P), we first
351 computed the power spectra during visual stimulation. Area 7A shows strong beta-band peaks in both
352 monkeys (Fig. 2E, F, monkey K: ≈ 17 Hz; monkey P: ≈ 13 Hz). Areas V1 and V4 show gamma
353 frequency peaks (Fig. 2A-D, monkey K: ≈ 76 Hz; monkey P: ≈ 60 Hz). Beta activity is visible in V4 and
354 V1 of both monkeys at their matching peak frequencies found in area 7A. In area V4 of both monkeys,

355 there are distinct beta peaks. In area V1, monkey K shows a distinct beta peak, and monkey P shows
356 a shoulder in the power spectrum, at the respective beta frequency.

357 We determined the dominant interareal communication frequencies for each monkey by calculating
358 the pair-wise phase consistency (PPC), a frequency-resolved measure of synchronization (Vinck et
359 al., 2010), between the V1-V4 and V1-7A ROI pairs (Fig. 2G-J). Gamma band synchronization was
360 present for both ROI pairs in both monkeys with peaks at ≈ 76 Hz in monkey K and in a range of 58–65
361 Hz in monkey P. Beta peaks were present between both ROI pairs: at ≈ 17 Hz in monkey K and at ≈ 12
362 Hz in monkey P. For the further analyses, data from both monkeys were combined, by aligning their
363 individual beta and gamma peaks ± 10 Hz and averaging across monkeys.

364 When determining individual beta and gamma frequencies, we selected the dominant peaks in the
365 respective frequency ranges. It has been shown that both beta and gamma frequencies show
366 substantial inter-individual variability, which can largely be explained by genetic factors (Vogel, 1970;
367 van Pelt et al., 2012). Note that while the beta peak in monkey P has its maximum at 12-13 Hz, at the
368 border between the alpha and beta band, the peak is strongly asymmetric with a sharp rise to the
369 maximal value and a slower falloff, such that most of the peak falls into the classical beta-frequency
370 band. This observation, together with the fact that it corresponded phenomenologically to the clear
371 beta peak in monkey K, led us to refer to it as beta, rather than alpha. The further analyses confirmed
372 that the beta rhythms in both monkeys exerted qualitatively the same effects. Yet whether they reflect
373 the same underlying physiological process cannot be determined on the basis of the ECoG recordings
374 alone. Some of the power and PPC spectra showed also a theta-band peak, which is not further
375 investigated, because the focus of this study is on the interaction between beta and gamma rhythms.

376 To demonstrate that interareal gamma-band synchronization is stimulus driven (Bosman et al., 2012;
377 Grothe et al., 2012), we contrasted PPC between the fixation and stimulation conditions. Figure 3A, B
378 shows significantly enhanced gamma-band synchronization between ROI pairs V1-V4 and 7A-V1
379 once the stimulus has appeared, in contrast to an almost flat spectrum when no stimulus is present.
380 This finding is consistent with gamma-band oscillations occurring as a result of stimulus drive. In
381 contrast, beta-band synchronization for both ROI pairs is present already during the pre-stimulus
382 fixation period, suggesting an endogenous origin (Fig. 3A, B). Beta synchronization is maintained
383 during the stimulation period, consistent with an ongoing top-down influence.

384 We next assessed the dominant directionality of interareal synchronization and its attentional
385 modulation. We quantified directionality of synchronization by means of Granger causality (GC)
386 (Granger, 1969; Ding et al., 2006; Bressler and Seth, 2011). As shown by Bastos et al. (2015c), and
387 extended to humans by Michalareas et al. (2016), the top-down beta-band influence of area 7A to V1
388 is significantly greater than the bottom-up beta-band influence of V1 to 7A (Fig. 3E). This top-down
389 beta-band influence is significantly increased when attention is directed to the visual hemifield
390 contralateral to the recording grid (Fig. 3C), consistent with an earlier report (Bastos et al., 2015c).
391 Between V1 and V4, the gamma-band influence is stronger in the bottom-up direction from area V1 to
392 V4 (Fig. 3F). The bottom-up gamma-band influence of V1 to V4 was significantly increased with
393 attention (Fig. 3D).

394 Note that the beta-band GC influence between V1 and V4 was stronger in the bottom-up than top-
395 down direction (Fig. 3F), in contrast to what has been reported for the same dataset (Bastos et al.,
396 2015c). This is due to differences in preprocessing between the present and the previous study. It
397 shows that for this particular pair of areas, the beta-band directionality is not robustly determined by
398 their hierarchical relationship. However, the difference in preprocessing did not affect other area pairs,
399 leaving the overall pattern intact, in which gamma-band influences are stronger in the bottom-up
400 direction and beta-band influences are stronger in the top-down direction. This overall pattern has also
401 been confirmed in an independent dataset from 43 human subjects (Michalareas et al., 2016), and in
402 this large human dataset, the beta-band influence between V1 and V4 also does not show an
403 unequivocal directionality, despite the overall pattern across all area pairs. Note that both in the
404 human MEG data, and in the macaque ECoG data presented here, V1-to-V4 GC did not significantly
405 exceed V4-to-V1 GC for all frequencies, that is, there was not a general broadband shift.

406 Top-Down Beta-Band Influences Correlate with Bottom-Up Gamma-Band Influences

407 Spontaneous endogenous increases in 7A-to-V1 beta GC may lead to increases in stimulus-driven
408 V1-to-V4 gamma GC. A resulting correlation between epoch-by-epoch fluctuations in the two GC
409 influences is difficult to quantify, because GC influences are not defined per single data epoch (without
410 substantially sacrificing spectral resolution and/or signal-to-noise ratio). To surmount this problem, we
411 used a jackknife approach. A jackknife replication (JR) of all epochs consists of all epochs except one,
412 that is, an all-but-one subsample of the epochs. There are as many JRs as there are epochs, because

413 each epoch can be left out once. If the GC in a given JR is high, this reflects a low GC in the left-out
414 epoch, and vice versa. This approach allows to median split epochs according to GC, and to sort and
415 bin epochs according to GC. Ultimately, it also allows to calculate the correlation between epoch-wise
416 top-down and bottom-up GC, a technique that we recently described and named Jackknife Correlation
417 (JC) (Richter et al., 2015).

418 We first investigate this for one example triplet of recording sites from monkey K. Data epochs were
419 median split based on the GC JRs. When we select the epochs in which V1-to-V4 gamma GC is
420 weak, 7A-to-V1 beta GC is almost absent; by contrast, when we select the epochs in which V1-to-V4
421 gamma GC is strong, 7A-to-V1 beta GC shows a pronounced peak (Fig.4A, left panel). A similar
422 dependency exists in the other direction. When we select epochs with weak 7A-to-V1 beta GC, V1-to-
423 V4 gamma GC is small; when we select epochs with strong 7A-to-V1 beta GC, V1-to-V4 gamma GC
424 is much larger (Fig. 4A, right panel). These results indicate a relationship between 7A-to-V1 beta GC
425 and V1-to-V4 gamma GC.

426 We next asked whether this relationship holds when we move from the coarse median split to finer
427 and finer bins, and calculate the Spearman rank correlation across bins. We sorted epochs according
428 to 7A-to-V1 beta GC JRs and binned them into 5, 10, 50 or 100 bins. Per bin, the 7A-to-V1 beta GC
429 JRs and the V1-to-V4 gamma GC JRs were averaged, and the correlation between them was
430 calculated across bins. This analysis revealed that the relationship found for the median split indeed
431 held for finer bins (Fig. 4B). Finally, we used JC to base the correlation analysis on single epochs,
432 which confirmed the relationship even at this most fine-grained level (Fig. 4B, rightmost bars). The
433 finer the binning, the lower the correlation value, and the lower the p-value, that is, the more significant
434 the correlation. This dependence of correlation and p-value on bin size has been previously described
435 as a general consequence of binning (Richter et al., 2015). Essentially, the widely-used sorting-and-
436 binning approach, through averaging observations per bin and thereby removing noise, leads to
437 dramatic increases in correlation values; yet this comes at the expense of statistical power and it
438 precludes an inference on the epoch-by-epoch correlation, which requires the JC approach.

439 To investigate the frequency-specificity of this correlation, JC was calculated between all possible
440 combinations of top-down and bottom-up frequencies, both ranging from 1-100 Hz. This analysis
441 revealed a correlation between 7A-to-V1 GC and V1-to-V4 GC in the beta band and in the gamma

442 band (Fig. 4C, lower left and upper right quadrants). Critically, and further confirming the median-split
443 and the sorting-and-binning analysis, 7A-to-V1 beta GC shows a significant positive correlation with
444 V1-to-V4 gamma GC (Fig. 4C, lower right quadrant). The peak of this cross-frequency interaction is
445 well aligned with the 7A-to-V1 beta and V1-to-V4 gamma GC peak frequencies (Figure 4C, dashed
446 lines). There is no significant JC between 7A-to-V1 gamma and V1-to-V4 beta GC, even though
447 7A-to-V1 gamma GC is significantly correlated to V1-to-V4 gamma GC, and 7A-to-V1 beta GC is
448 significantly correlated to V1-to-V4 beta GC.

449 We then repeated these analyses for all possible triplets (Fig. 5). Figure 5A, B, C uses the same
450 format as Figure 4A, B, C, but shows the grand average over all triplets and the two monkeys after
451 alignment by their respective top-down beta, and bottom-up gamma peak frequencies. The pattern of
452 results found for the example triplet held in the grand average, even though average effect size was
453 smaller. Figure 5D shows the probability distribution across triplets of JC values between 7A-to-V1
454 beta GC and V1-to-V4 gamma GC, averaged over monkeys. The distribution shows a positive skew
455 and greater mass above zero, indicating a greater number and magnitude of positive correlations,
456 though with a substantial number of negative correlations, which partially accounts for the low average
457 JC value.

458 To determine whether greater GC values resulted in greater JC values, we weighted the JC value of
459 each triplet by the product of the respective triplet's top-down beta and bottom-up gamma GC values,
460 followed by averaging over triplets. This resulted in an increase of the mean JC value from 0.006 to
461 0.014, that is, a $\approx 230\%$ increase ($p < 0.001$, two-tailed non-parametric randomization test). This
462 indicates that site pairs with larger GC magnitudes, which are less susceptible to the influence of
463 noise, give rise to higher correlation coefficients.

464 Next, we tested whether the correlation was affected by attentional state. We calculated the JC
465 between 7A-to-V1 beta GC and V1-to-V4 gamma GC, separately for the attend-contra and attend-ipsi
466 conditions. The JC was significant for each attention condition separately ($p < 0.001$). Selective
467 attention to the right hemifield stimulus, activating the recorded left hemisphere, enhanced JC values
468 by 17% (attend-contra: 0.007; attend-ipsi: 0.006, $p = 0.006$, two-tailed paired non-parametric
469 randomization test). This effect is likely related to the observed increase in JC, when triplets are

470 weighted by GC values, because attention increased both 7A-to-V1 beta GC and V1-to-V4 gamma
471 GC (Fig. 3 C, D).

472 The sorting-and-binning analysis showed that the JC increases substantially when 7A-to-V1 GC and
473 V1-to-V4 GC are averaged per bin, thereby removing noise across individual triplets within bins. The
474 bin-wise averaging precludes an inference on the epoch-by-epoch correlation. Therefore, we explored
475 an alternative approach to reduce noise, while retaining an epoch-by-epoch correlation. Per epoch, we
476 averaged GC JRs over all 7A-to-V1 site pairs, and we averaged GC JRs over all V1-to-V4 site pairs.
477 Thus, per monkey, we constructed one triplet comprising the average 7A-to-V1 GC and the average
478 V1-to-V4 GC. Figure 6A, B, C shows the resulting analyses in the same format as the respective
479 panels in Figures 4 and 5. After reduction of noise across site pairs, the pattern of results was
480 confirmed, yet with substantially increased correlation values. Importantly, this also holds for the
481 epoch-wise JC values shown in the rightmost bars of Figure 6B and in Figure 6C. The JC value
482 between 7A-to-V1 beta GC and V1-to-V4 gamma GC increased from 0.006 in the average across
483 individual triplets to 0.12, that is, it showed a 20-fold increase. This is a striking demonstration of the
484 utility of spatial averaging for exposing the epoch-wise correlation. When we additionally give up the
485 epoch-wise calculation and smooth the GC values further through binning of epochs, correlations
486 increase even more and exceed values of 0.6 for a typical 10-bin scheme (Fig. 6 B).

487 To investigate whether V1-to-V4 gamma GC is truly dependent on 7A-to-V1 beta GC influences,
488 rather than merely on 7A beta power, we stratified for beta power. We applied this to the median split
489 analysis, because it lends itself best to stratification. As before, we median split epochs based on 7A-
490 to-V1 beta GC JRs. The 7A power spectra aligned to the monkeys' individual beta peak frequencies
491 showed that stronger 7A-to-V1 beta GC was in fact related to higher 7A beta power (Fig. 6D, left
492 panel, solid lines). This power difference is fully in line with the hypothesis that the top-down beta-
493 band influence is generated in 7A. Power differences were sufficiently small, such that stratification
494 rendered the power spectra almost identical (Fig. 6D, left panel, dashed lines). After stratification, V1-
495 to-V4 gamma-band GC values remained almost unchanged compared to the values before
496 stratification (compare right panels of Fig. 6A and D). Thus, V1-to-V4 gamma GC depended not on 7A
497 power differences, but rather on actual 7A-to-V1 GC influences through synchronization.

498 Spatial Resolution of the Correlation between Top-Down and Bottom-Up Influences

499 We next investigated whether the JC between 7A-to-V1 beta GC and V1-to-V4 gamma GC depended
500 on involving the same V1 site, which would demonstrate spatial specificity at the level of recording
501 sites. We tested this spatial specificity by pairing 7A-to-V1 beta GC to a specific V1 site, with V1-to-V4
502 gamma GC from a different V1 site. The distance that separated the two V1 sites was parametrically
503 varied. For each V1 site, 5 sets of other V1 sites were defined that fell into pre-specified distance
504 intervals (1 cm per interval, stepped by 2.5 mm, between 0 and 2 cm). Figure 7A shows one example
505 V1 site (arrow) and illustrates with 5 colored lines the five distance intervals (colored lines were slightly
506 displaced for illustration purposes). The average distance for each distance interval is marked with a
507 filled circle. Figure 7B shows the resulting JCs, averaged over triplets and monkeys, as a function of
508 distance. It can be seen that as the distance between the two V1 sites increases, there is a monotonic
509 falloff of the correlation coefficient between 7A-to-V1 beta and V1-to-V4 gamma GC. This indicates
510 that the physiological process linking 7A-to-V1 beta GC to V1-to-V4 gamma GC is not global, but
511 rather spatially specific. As a consequence, any spatially non-specific fluctuations, for example of
512 neuromodulators reflecting arousal fluctuations, are unlikely to cause the observed correlation.

513 Top-down Beta Leads Bottom-up Gamma in Time

514 We have established that spontaneous fluctuations in endogenous top-down beta GC are correlated
515 with fluctuations in stimulus-driven bottom-up gamma GC. To investigate whether the data contain
516 evidence in support of a causal relation, we assessed whether top-down beta GC is predictive of
517 subsequent bottom-up gamma GC. To accomplish this, we extended the JC by adding a temporal
518 dimension, similar to time-lagged cross-correlation. We compute the JC on time-frequency data,
519 where we systematically offset 7A-to-V1 beta GC JRs from V1-to-V4 gamma GC JRs by positive or
520 negative lags. We call this procedure lagged jackknife correlation (LJC). This quantifies at what time
521 delay between the top-down beta-band influence and the bottom-up gamma-band influence the JC
522 between them is largest. We computed LJC for each triplet. The red curve in Figure 8 shows the LJC
523 averaged over triplets and monkeys and exhibits a peak at -0.105 s, indicating that 7A-to-V1 beta GC
524 led V1-to-V4 gamma GC by 0.105 s ($t(10663) = -7.576$, $p \ll 0.001$, two-tailed jackknife-based t-test).
525 The LJC dropped off slowly, which likely reflects slow dynamics of the underlying GC influences
526 together with the fact that the windows used for GC influence estimation result in low-pass filtering of

527 GC influence time courses. For comparison, we performed the same LJC analysis between 7A-to-V1
528 gamma GC and V1-to-V4 beta GC. This combination had not shown a significant correlation in the
529 non-lagged case (Fig. 5C, upper left quadrant), which was confirmed for the lagged case (Fig. 8, gray
530 line).

531 Discussion

532 We used LFP recordings from 252-channel ECoG arrays covering large parts of the left hemispheres
533 of two macaques to analyze the interaction between top-down and bottom-up influences, both
534 quantified by Granger-causality (GC). Top-down influences were assessed between area 7a at the top
535 of the visual hierarchy and V1 at the bottom. Bottom-up influences were assessed between V1 and
536 V4, a known feedforward pathway carrying stimulus driven input. 7A-to-V1 GC showed a beta-band
537 peak, which did not require visual stimulation and thus was endogenously generated, which was
538 significantly larger in the 7A-to-V1 than the V1-to-7A direction, and which increased with selective
539 attention. V1-to-V4 GC showed a gamma-band peak, which was stimulus driven, which was
540 significantly larger in the bottom-up than the top-down direction, and which also increased with
541 selective attention. Jackknife Correlation between top-down beta-band influences and bottom-up
542 gamma-band influences revealed a positive cross-frequency interaction. This interaction was spatially
543 specific, as it was maximal between top-down and bottom-up interareal influences that shared the
544 same V1 site. Finally, top-down beta-band influences best predicted bottom-up gamma-band
545 influences ~ 0.1 s later, suggesting that the cross-frequency interaction is causal. Therefore, we
546 conclude that 7A-to-V1 beta-band influences enhance V1-to-V4 gamma-band influences.

547 Noise can affect GC estimates (Nalatore et al., 2007; Vinck et al., 2015). Fluctuating shared noise
548 could in principle generate correlation between GC fluctuations. Yet, a predominant source of shared
549 noise, volume conduction, is strongly attenuated in our signals due to bipolar derivation
550 (Trongnetrpunya et al., 2015). Furthermore, influences of shared noise on the two GC metrics should
551 typically occur nearly simultaneously and therefore, the lagged JC would peak at zero-lag, whereas
552 we found a significant lag of ~ 0.1 s. Also, local noise can affect GC estimates, yet these effects do not
553 necessarily explain a positive correlation between GC influences. For example, enhanced noise in a
554 recording site can lead to an overestimation of the GC influence onto that site, and at the same time to

555 an underestimation of the GC influence of that site onto other sites (Bastos and Schoffelen, 2015a). If
556 this applied to our V1 recording sites, fluctuations in their noise level would artefactually reduce the
557 observed correlation and thereby lead to an underestimation of the true correlation value. Finally, the
558 observed increase in average JC after weighting site triplets by the GC values of their constituent site
559 pairs argues against a confounding role of noise. The effect of noise on GC is larger for weaker GC.
560 Thus, if noise had generated the observed JC, more weight for strong-GC triplets would have reduced
561 the average JC. By contrast, we observed an increased average JC, which is consistent with our
562 interpretation of actual top-down influences affecting actual bottom-up influences.

563 Additional alternative scenarios concern physiological modulatory effects that act independently on
564 both, 7A-to-V1 beta GC and V1-to-V4 gamma GC, without a direct causal link between the two GC
565 influences. Those interareal GC influences can probably only be affected at the circuits containing the
566 respective projection neurons and at the circuits containing their postsynaptic target neurons, that is,
567 not at the corresponding interareal axonal projections. Thus, to explain our observations, such
568 modulatory effects would need to modify 7A circuits to enhance their beta outflow, and 0.1 s thereafter
569 modify V1 circuits to enhance their gamma outflow. Alternatively, they would need to modify V1
570 circuits to enhance their beta susceptibility, and 0.1 s thereafter modify V4 circuits to enhance their
571 gamma susceptibility. Additional mechanisms would be necessary to explain the observed spatial
572 specificity. Thus, these alternative interpretations require complex sets of assumptions. Certainly,
573 widespread or even global neuromodulatory fluctuations, as potentially associated with arousal
574 fluctuations, cannot explain the observed pattern of results.

575 The most parsimonious interpretation seems to be the following: The 7A-to-V1 beta-band influence
576 onto a given V1 site enhances with 0.1 s delay that site's V1-to-V4 gamma influence. We propose that
577 this cross-frequency interaction constitutes a mechanism for spatially selective attention. If correct, this
578 entails that the top-down control of selective attention corresponds fully or partly to top-down beta-
579 band influences, and the ensuing preferential bottom-up routing of the attentionally selected stimulus
580 corresponds fully or partly to bottom-up gamma-band influences. Thus, epoch-by-epoch fluctuations in
581 spatially selective attention could well generate the observed correlations. In fact, we would like to
582 identify the epoch-by-epoch GC fluctuations that are the basis for the observed correlations with
583 epoch-by-epoch fluctuations of spatially selective attention. Several recent studies have revealed that

584 attention samples stimuli rhythmically, with a predominant sampling rhythm in the theta and/or alpha
585 range (7-13 Hz), which is multiplexed across the sampled stimuli (Landau and Fries, 2012; Fiebelkorn
586 et al., 2013; Holcombe and Chen, 2013; Fries, 2015; Landau et al., 2015; VanRullen, 2016). Future
587 studies will need to investigate whether the correlations described here are specifically driven by those
588 attentional sampling rhythms.

589 Numerous studies in visual cortex have reported gamma-band synchronization within and between
590 visual areas (Gray and Singer, 1989; Engel et al., 1991; Kreiter and Singer, 1996; Tallon-Baudry et al.,
591 1996; Fries et al., 1997; Fries, 2001; Bichot et al., 2005; Taylor et al., 2005; Hoogenboom et al., 2006;
592 Womelsdorf et al., 2006; Wyart and Tallon-Baudry, 2008), and numerous studies in parietal cortex
593 have reported beta-band synchronization within parietal areas and between parietal and frontal areas
594 (Buschman and Miller, 2007; Salazar et al., 2012; Dotson et al., 2014; Stetson and Andersen, 2014).
595 Recent ECoG recordings covering both visual and parietal areas revealed that interareal beta-band
596 influences predominate in the top-down and interareal gamma-band influences predominate in the
597 bottom-up direction (Bastos et al., 2015c). These findings link parietal beta-band activity with visual
598 gamma-band activity and suggest a concrete case of cross-frequency interaction (Bressler and
599 Richter, 2015). In the present paper, we have tested some of the resulting predictions and found direct
600 experimental support for such a cross-frequency interaction that allows top-down beta-band influences
601 to enhance bottom-up gamma-band influences.

602 Cortical anatomy has revealed a distinct laminar pattern of top-down and bottom-up projections
603 (Felleman and Van Essen, 1991; Markov et al., 2014). Bottom-up projections originate predominantly
604 in superficial layers, and this predominance increases with the number of hierarchical levels bridged
605 by the bottom-up projection. Note that an additional bottom-up pathway via the pulvinar originates in
606 layer 5, and it might mediate the observed V1-to-V4 GC influences in the beta band (Shipp, 2003;
607 Sherman, 2007; Schmid et al., 2012). Furthermore, bottom-up projections terminate predominantly in
608 layer 4. Top-down projections originate predominantly in deep layers, and this predominance
609 increases with the number of hierarchical levels bridged by the top-down projection. Furthermore, top-
610 down projections terminate predominantly outside layer 4, primarily in layers 1 and 6. Determining how
611 the respective top-down influences interact with local processing, and thereby ultimately with bottom-
612 up influences, remains a central neuroscientific quest. One potential mechanism has been proposed in

613 a model that entails details of both layer-specific anatomy and cellular biophysics (Lee et al., 2013),
614 and that replicates the effect of top-down selective attention on bottom-up gamma-band coherence.
615 The model implicates a subclass of inhibitory interneurons, the slow-inhibitory (SI) interneurons, as
616 targets of top-down modulation. These cells may span multiple cortical laminae and thus are suitably
617 situated for integration of neuronal activity across layers. A subpopulation of these cells, low-threshold
618 spiking (LTS) cells, are found in deep layers of the cortex. In the model, LTS cells: 1) are hypothesized
619 to receive top-down input, 2) are implicated in the generation of beta oscillations and in a resonant
620 response to beta-rhythmic top-down input, 3) selectively modulate gamma-band activation in layer 2/3,
621 leading to an enhanced gamma band output. Our present analysis confirms the central prediction of
622 the Lee et al. (2013) paper, namely that specifically top-down beta-band influences enhance stimulus-
623 driven gamma-band processes. Lee et al. show how this mechanism can support the implementation
624 of attentional stimulus selection. The current results, which mechanistically link the previously reported
625 attentional enhancements of top-down beta and bottom-up gamma influences, provide the hitherto
626 missing experimental bridge. Together, experiments, modeling and model-testing data analysis have
627 led to an intriguingly coherent understanding of the neuronal processes behind the implementation of
628 attentional stimulus selection.

629 References

- 630 Bastos AM, Schoffelen J-M (2015a) A Tutorial Review of Functional Connectivity Analysis
631 Methods and Their Interpretational Pitfalls. *Front Syst Neurosci* 9:175.
- 632 Bastos AM, Usrey WM, Adams RA, Mangun GR, Fries P, Friston KJ (2012) Canonical
633 microcircuits for predictive coding. *Neuron* 76:695–711.
- 634 Bastos AM, Litvak V, Moran R, Bosman CA, Fries P, Friston KJ (2015b) A DCM study of
635 spectral asymmetries in feedforward and feedback connections between visual areas V1 and
636 V4 in the monkey. *Neuroimage* 108:460–475.
- 637 Bastos AM, Vezoli J, Bosman CA, Schoffelen J-M, Oostenveld R, Dowdall JR, De Weerd P,
638 Kennedy H, Fries P (2015c) Visual areas exert feedforward and feedback influences through
639 distinct frequency channels. *Neuron* 85:390–401.
- 640 Bichot NP, Rossi AF, Desimone R (2005) Parallel and serial neural mechanisms for visual
641 search in macaque area V4. *Science* 308:529–534.
- 642 Bieri KW, Bobbitt KN, Colgin LL (2014) Slow and fast γ rhythms coordinate different spatial
643 coding modes in hippocampal place cells. *Neuron* 82:670–681.
- 644 Bisley JW, Goldberg ME (2003) Neuronal Activity in the Lateral Intraparietal Area and Spatial
645 Attention. *Science* 299:81–86.
- 646 Bosman CA, Schoffelen J-M, Brunet N, Oostenveld R, Bastos AM, Womelsdorf T, Rubehn B,
647 Stieglitz T, De Weerd P, Fries P (2012) Attentional Stimulus Selection through Selective
648 Synchronization between Monkey Visual Areas. *Neuron* 75:875–888.
- 649 Bressler SL, Richter CG (2015) Interareal oscillatory synchronization in top-down neocortical
650 processing. *Curr Opin Neurobiol* 31:62–66.
- 651 Bressler SL, Seth AK (2011) Wiener-Granger causality: a well established methodology.
652 *Neuroimage* 58:323–329.
- 653 Brunet N, Bosman CA, Vinck M, Roberts M, Oostenveld R, Desimone R, De Weerd P, Fries P
654 (2014a) Stimulus repetition modulates gamma-band synchronization in primate visual
655 cortex. *Proc Natl Acad Sci USA* 111:3626–3631.
- 656 Brunet N, Vinck M, Bosman CA, Singer W, Fries P (2014b) Gamma or no gamma, that is the
657 question. *Trends Cogn Sci (Regul Ed)* 18:507–509.
- 658 Brunet N, Bosman CA, Roberts M, Oostenveld R, Womelsdorf T, De Weerd P, Fries P
659 (2015) Visual Cortical Gamma-Band Activity During Free Viewing of Natural Images. *Cereb*
660 *Cortex* 25:918–926.
- 661 Buschman TJ, Miller EK (2007) Top-down versus bottom-up control of attention in the
662 prefrontal and posterior parietal cortices. *Science* 315:1860–1862.
- 663 Colgin LL, Denninger T, Fyhn M, Hafting T, Bonnevie T, Jensen O, Moser M-B, Moser EI
664 (2009) Frequency of gamma oscillations routes flow of information in the hippocampus.
665 *Nature* 462:353–357.

- 666 Dhamala M, Rangarajan G, Ding M (2008) Analyzing information flow in brain networks with
667 nonparametric Granger causality. *Neuroimage* 41:354–362.
- 668 Ding M, Chen Y, Bressler SL (2006) Granger Causality: Basic Theory and Application to
669 Neuroscience Schelter B, Winterhalder M, Timmer J, eds. *Handbook of Time Series
670 Analysis: Recent Theoretical Developments and Applications*.
- 671 Dotson NM, Salazar RF, Gray CM (2014) Frontoparietal correlation dynamics reveal
672 interplay between integration and segregation during visual working memory. *34:13600–
673 13613*.
- 674 Efron B (1981) Nonparametric estimates of standard error: The jackknife, the bootstrap and
675 other methods. *Biometrika*.
- 676 Efron B, Tibshirani RJ (1994) *An Introduction to the Bootstrap*. Boca Raton: CRC Press.
- 677 Engel AK, Kreiter AK, König P, Singer W (1991) Synchronization of oscillatory neuronal
678 responses between striate and extrastriate visual cortical areas of the cat. *Proc Natl Acad Sci
679 USA* 88:6048–6052.
- 680 Felleman D, Van Essen DC (1991) Distributed hierarchical processing in the primate cerebral
681 cortex. *Cereb Cortex* 1:1–47.
- 682 Fiebelkorn IC, Saalman YB, Kastner S (2013) Rhythmic Sampling within and between
683 Objects despite Sustained Attention at a Cued Location. *Curr Biol* 23:2553–2558.
- 684 Fontolan L, Morillon B, Liegeois-Chauvel C, Giraud A-L (2014) The contribution of frequency-
685 specific activity to hierarchical information processing in the human auditory cortex. *Nat
686 Commun* 5:4694.
- 687 Fries P (2001) Modulation of Oscillatory Neuronal Synchronization by Selective Visual
688 Attention. *Science* 291:1560–1563.
- 689 Fries P (2015) Rhythms for Cognition: Communication through Coherence. *Neuron* 88:220–
690 235.
- 691 Fries P, Roelfsema PR, Engel AK, König P, Singer W (1997) Synchronization of oscillatory
692 responses in visual cortex correlates with perception in interocular rivalry. *Proc Natl Acad Sci
693 USA* 94:12699–12704.
- 694 Gilbert CD, Sigman M (2007) Brain states: top-down influences in sensory processing.
695 *Neuron* 54:677–696.
- 696 Granger C (1969) Investigating causal relations by econometric models and cross-spectral
697 methods. *Econometrica* 37:424–438.
- 698 Gray CM, Singer W (1989) Stimulus-specific neuronal oscillations in orientation columns of
699 cat visual cortex. *Proc Natl Acad Sci USA* 86:1698–1702.
- 700 Grothe I, Neitzel SD, Mandon S, Kreiter AK (2012) Switching neuronal inputs by differential
701 modulations of gamma-band phase-coherence. *32:16172–16180*.
- 702 Hilgetag CC, O'Neill MA, Young MP (1996) Indeterminate organization of the visual system.
703 *Science* 271:776–777.

- 704 Holcombe AO, Chen W-Y (2013) Splitting attention reduces temporal resolution from 7 Hz for
705 tracking one object to <3 Hz when tracking three. *J Vis* 13:12–12.
- 706 Hoogenboom N, Schoffelen J-M, Oostenveld R, Parkes LM, Fries P (2006) Localizing human
707 visual gamma-band activity in frequency, time and space. *Neuroimage* 29:764–773.
- 708 Jia X, Tanabe S, Kohn A (2013) Gamma and the Coordination of Spiking Activity in Early
709 Visual Cortex. *Neuron* 77:762–774.
- 710 Kreiter AK, Singer W (1996) Stimulus-dependent synchronization of neuronal responses in
711 the visual cortex of the awake macaque monkey. *16:2381–2396*.
- 712 Landau AN, Fries P (2012) Attention Samples Stimuli Rhythmically. *Curr Biol* 22:1000–1004.
- 713 Landau AN, Schreyer HM, van Pelt S, Fries P (2015) Distributed Attention Is Implemented
714 through Theta-Rhythmic Gamma Modulation. *Curr Biol* 25:2332–2337.
- 715 Lee JH, Whittington MA, Kopell NJ (2013) Top-down beta rhythms support selective attention
716 via interlaminar interaction: a model. *PLoS Comput Biol* 9:e1003164.
- 717 Lewis CM, Bosman CA, Womelsdorf T, Fries P (2016) Stimulus-induced visual cortical
718 networks are recapitulated by spontaneous local and interareal synchronization. *Proc Natl
719 Acad Sci USA* 113:E606–E615.
- 720 Maris E, Oostenveld R (2007) Nonparametric statistical testing of EEG- and MEG-data. *J
721 Neurosci Methods* 164:177–190.
- 722 Markov NT, Vezoli J, Chameau P, Falchier A, Quilodran R, Huissoud C, Lamy C, Misery P,
723 Giroud P, Ullman S, Barone P, Dehay C, Knoblauch K, Kennedy H (2014) Anatomy of
724 hierarchy: feedforward and feedback pathways in macaque visual cortex. *J Comp Neurol*
725 522:225–259.
- 726 Michalareas G, Vezoli J, van Pelt S, Schoffelen J-M, Kennedy H, Fries P (2016) Alpha-Beta
727 and Gamma Rhythms Subserve Feedback and Feedforward Influences among Human
728 Visual Cortical Areas. *Neuron* 89:384–397.
- 729 Nichols TE, Holmes AP (2002) Nonparametric permutation tests for functional neuroimaging:
730 a primer with examples. *Hum Brain Mapp* 15:1–25.
- 731 Oostenveld R, Fries P, Maris E, Schoffelen J-M (2011) FieldTrip: Open source software for
732 advanced analysis of MEG, EEG, and invasive electrophysiological data. *Comput Intell
733 Neurosci* 2011:156869.
- 734 Paxinos G, Huang X, Toga AW (1999) *The Rhesus Monkey Brain in Stereotaxic
735 Coordinates*. San Diego: Academic Press.
- 736 Percival DB, Walden AT (1993) *Spectral Analysis for Physical Applications*. Cambridge
737 University Press.
- 738 Pinotsis DA, Brunet N, Bastos A, Bosman CA, Litvak V, Fries P, Friston KJ (2014) Contrast
739 gain control and horizontal interactions in V1: A DCM study. *Neuroimage* 92:143–155.
- 740 Richter CG, Thompson WH, Bosman CA, Fries P (2015) A jackknife approach to quantifying
741 single-trial correlation between covariance-based metrics undefined on a single-trial basis.

- 742 Neuroimage 114:57–70.
- 743 Rohlfing T, Kroenke CD, Sullivan EV, Dubach MF, Bowden DM, Grant KA, Pfefferbaum A
744 (2012) The INIA19 Template and NeuroMaps Atlas for Primate Brain Image Parcellation and
745 Spatial Normalization. *Front Neuroinform* 6:27.
- 746 Rubehn B, Bosman C, Oostenveld R, Fries P, Stieglitz T (2009) A MEMS-based flexible
747 multichannel ECoG-electrode array. *J Neural Eng* 6:036003.
- 748 Salazar RF, Dotson NM, Bressler SL, Gray CM (2012) Content-specific fronto-parietal
749 synchronization during visual working memory. *Science* 338:1097–1100.
- 750 Schmid MC, Singer W, Fries P (2012) Thalamic Coordination of Cortical Communication.
751 *Neuron* 75:551–552.
- 752 Sherman SM (2007) The thalamus is more than just a relay. *Current Opinion in Neurobiology*
753 17:417–422.
- 754 Shipp S (2003) The functional logic of cortico–pulvinar connections. *Philos Trans R Soc Lond*
755 *B Biol Sci* 358:1605–1624.
- 756 Sirota, A., Montgomery, S., Fujisawa, S., Isomura, Y., Zugaro, M., and Buzsaki, G.
757 (2008) Entrainment of neocortical neurons and gamma oscillations by the hippocampal theta
758 rhythm. *Neuron* 60:683-697.
759
- 760 Stetson C, Andersen RA (2014) The parietal reach region selectively anti-synchronizes with
761 dorsal premotor cortex during planning. 34:11948–11958.
- 762 Tallon-Baudry C, Bertrand O, Delpuech C, Pernier J (1996) Stimulus specificity of phase-
763 locked and non-phase-locked 40 Hz visual responses in human. 16:4240–4249.
- 764 Taylor K, Mandon S, Freiwald WA, Kreiter AK (2005) Coherent oscillatory activity in monkey
765 area v4 predicts successful allocation of attention. *Cereb Cortex* 15:1424–1437.
- 766 Thomson DJ (1977) Spectrum Estimation Techniques for Characterization and Development
767 of WT4 Waveguide-I. *Bell System Technical Journal* 56:1769–1815.
- 768 Thomson DJ (1982) Spectrum estimation and harmonic analysis. *Proceedings of the IEEE*
769 70:1055–1096.
- 770 Trongnetrpunya A, Nandi B, Kang D, Kocsis B, Schroeder CE, Ding M (2015) Assessing
771 Granger Causality in Electrophysiological Data: Removing the Adverse Effects of Common
772 Signals via Bipolar Derivations. *Front Syst Neurosci* 9:189.
- 773 Van Essen DC (2012) Cortical cartography and Caret software. *Neuroimage* 62:757–764.
- 774 van Kerkoerle T, Self MW, Dagnino B, Gariel-Mathis M-A, Poort J, van der Togt C,
775 Roelfsema PR (2014) Alpha and gamma oscillations characterize feedback and feedforward
776 processing in monkey visual cortex. *Proc Natl Acad Sci USA* 111:14332–14341.
- 777 van Pelt S, Boomsma DI, Fries P (2012) Magnetoencephalography in twins reveals a strong
778 genetic determination of the peak frequency of visually induced γ -band synchronization. *J*
779 *Neurosci* 32:3388–3392.

- 780 VanRullen R (2016) Perceptual Cycles. *Trends Cogn Sci (Regul Ed)* 20:723–735.
- 781 Vinck M, Huurdeman L, Bosman CA, Fries P, Battaglia FP, Pennartz CMA, Tiesinga PH
782 (2015) How to detect the Granger-causal flow direction in the presence of additive noise?
783 *Neuroimage* 108:301–318.
- 784 Vinck M, van Wingerden M, Womelsdorf T, Fries P, Pennartz CMA (2010) The pairwise
785 phase consistency: a bias-free measure of rhythmic neuronal synchronization. *Neuroimage*
786 51:112–122.
- 787 Vogel F (1970) The genetic basis of the normal human electroencephalogram (EEG).
788 *Humangenetik* 10:91–114.
- 789 von Stein A, Sarnthein J (2000) Different frequencies for different scales of cortical
790 integration: from local gamma to long range alpha/theta synchronization. *Int J Psychophysiol*
791 38:301–313.
- 792 Welch P (1967) The use of fast Fourier transform for the estimation of power spectra: A
793 method based on time averaging over short, modified periodograms. *IEEE Trans Audio*
794 *Electroacoust* 15:70–73.
- 795 Womelsdorf T, Fries P, Mitra PP, Desimone R (2006) Gamma-band synchronization in visual
796 cortex predicts speed of change detection. *Nature* 439:733–736.
- 797 Wyart V, Tallon-Baudry C (2008) Neural dissociation between visual awareness and spatial
798 attention. *28:2667–2679*.
- 799
- 800

801 Figure Legends

802 **Figure 1.** Behavioral task and recording locations. **A**, The task commenced with a fixation period
803 followed by presentation of two differently colored stimuli. The fixation point color then indicated the
804 visual stimulus to covertly attend in either the visual hemifield ipsilateral (attend-ipsi) or contralateral
805 (attend-contra) to the recording grid. The presentation timings for each monkey are shown as a
806 timeline. **B**, Recording sites for areas V1 and V2 (red), V4 (blue), and 7A (yellow) from monkey K (light
807 gray spheres) and monkey P (black spheres), co-registered to a common macaque template.

808 **Figure 2.** Power spectra and phase locking (PPC) spectra during visual stimulation. V4 (**A, B**), V1 (**C**,
809 **D**), and 7A (**E, F**) power spectra averaged over all respective site pairs of monkey K (**A, C, E**) and P
810 (**B, D, F**). Power values at each frequency were multiplied by that frequency value to reduce the 1/f
811 component. (**G-J**) LFP-LFP PPC for V1-V4 (**G, H**) and V1-7A (**I, J**), for monkey K (**G, I**) and P (**H, J**),
812 respectively. Error regions show ± 1 standard error of the mean (SEM) over sites or site pairs.
813 Frequencies from 45-55 Hz were omitted due to line-noise pollution.

814 **Figure 3.** Average phase locking (PPC) and Granger causality (GC) spectra. All spectra were first
815 averaged over site pairs, then over monkeys after alignment to their beta and gamma peak
816 frequencies. **A**, LFP-LFP PPC for 7A-V1 and **B**, V1-V4 during fixation (dark shading) and visual
817 stimulation (light shading). Error regions show ± 1 standard error of the mean (SEM) over site pairs,
818 merely for illustration. Gray background shading indicates frequency regions with significant condition
819 differences ($p < 0.05$, two-tailed non-parametric randomization test, corrected for comparisons across
820 multiple frequencies). Inset brackets denote the minimum separation required for significance. **C**,
821 7A-to-V1 GC influence spectra and **D**, V1-to-V4 GC influence spectra, for attend-contra (light shading)
822 and attend-ipsi (dark shading). Same statistics conventions as **A** and **B**. **E**, Bidirectional GC influences
823 for 7A-V1 and **F**, V1-V4. For 7A-V1, the 7A-to-V1 influences are shown in blue shading, and the V1-to-
824 7A influences in dark shading. For V1-V4, V1-to-V4 influences are shown in green shading, and V4-to-
825 V1 influences in light shading. Same statistics conventions as **A** and **B**, but with statistical tests based
826 on a non-parametric bootstrap procedure. **G**, Top-down modulatory stream (blue arrow) from
827 7A-to-V1, and bottom-up feedforward path from V1-to-V4 (green arrow).

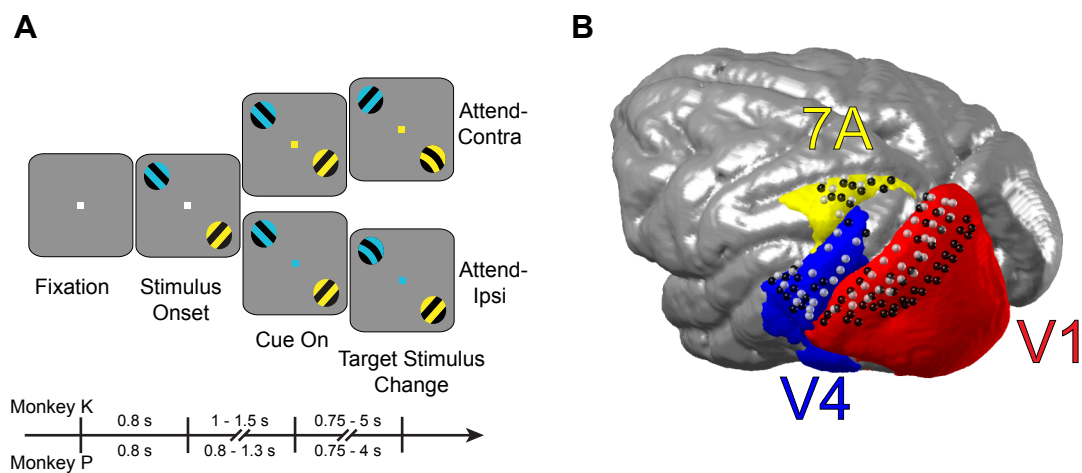
828 **Figure 4.** Example triplet: Median split, correlation across binned epochs, and JC. **A**, left panel:
829 7A-to-V1 GC for epochs median split by the V1-to-V4 gamma GC jackknife replications; right panel:
830 V1-to-V4 GC for epochs median split by the 7A-to-V1 beta GC jackknife replications. Gray background
831 shading indicates significant differences ($p < 0.05$, two-tailed non-parametric randomization test,
832 corrected for multiple comparisons across frequencies). Inset brackets denote the minimum
833 separation required for significance. **B**, The correlation between 7A-to-V1 beta GC and V1-to-V4
834 gamma GC for the sorted data divided into 5, 10, 50, or 100 bins, and without binning. Corresponding
835 p-values for each correlation coefficient are shown below with a dashed line marking $p = 0.05$. **C**, The 4
836 colored panels show JC for the selected 7A-to-V1-to-V4 triplet. The frequencies of 7A-to-V1 GC are
837 shown on the vertical axis, the frequencies of V1-to-V4 GC are shown on the horizontal axis. The
838 frequency ranges 1-50 Hz and 51-100 Hz are shown separately, because they required slightly
839 different spectral analyses (see Materials and Methods). Non-significant regions are partially masked
840 by white ($p < 0.001$, two-tailed non-parametric randomization test, corrected for multiple comparisons
841 across both frequency axes). The line plots at the bottom show the GC spectrum for the
842 corresponding V1-to-V4 site pair. The line plots to the left show the GC spectrum for the
843 corresponding 7A-to-V1 site pair. Dashed lines mark the top-down beta GC spectral peak and the
844 bottom-up gamma GC spectral peak.

845 **Figure 5.** Average over all triplets and both monkeys: Median split, correlation across binned epochs,
846 and JC. (**A**, **B**, **C**) Same format as Figure 4A, B, C, but averaging over all triplets and both monkeys,
847 after aligning to their individual beta and gamma peak frequencies. **D**, Probability distribution across
848 triplets of JC values between 7A-to-V1 beta GC and V1-to-V4 gamma GC, averaged over monkeys.

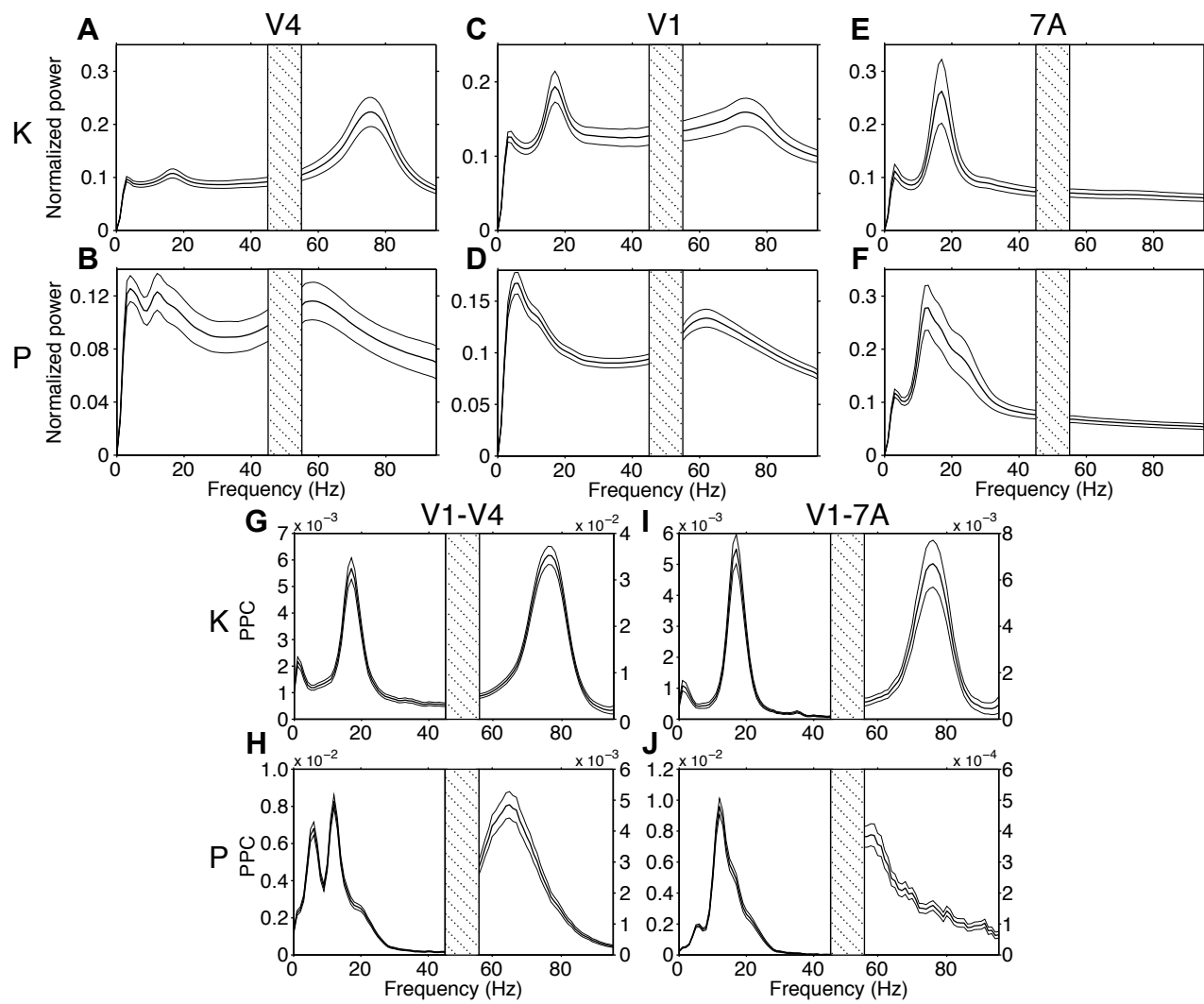
849 **Figure 6.** Triplet based on average 7A-to-V1 GC and average V1-to-V4 GC: Median split, correlation
850 across binned epochs, and JC. (**A**, **B**, **C**) Same format as Figure 5A, B, C, but for a triplet formed by
851 the average 7A-to-V1 GC jackknife replications and the average V1-to-V4 GC jackknife replications,
852 per monkey, and then averaged over monkeys. **D**, Left panel: 7A beta-band power spectra after
853 median split by 7A-to-V1 beta GC jackknife replications. Solid lines: Before stratification; Dashed lines:
854 After stratification. Right panel: Same as right panel of **A**, but after stratification for 7A beta power.

855 **Figure 7.** Spatial specificity of correlation between top-down beta and bottom-up gamma GC. **A**, Inset:
856 MRI of monkey K with the surgical trepanation and prominent sulci overlaid. The blow-up shows
857 recording sites in 7A (yellow), V1 (red), and V4 (blue) that were analyzed. The V1 site marked by the
858 arrow serves as an example to demonstrate the distance intervals from which another V1 site may
859 have been chosen, which were 0 to 1 cm (magenta), 0.25 to 1.25 cm (orange), 0.5 to 1.5 cm (yellow),
860 0.75 to 1.75 cm (green), and 1 to 2 cm (cyan). Solid circles mark the average distance between V1
861 sites that were chosen for each distance interval. The particular arrangement of the distance intervals
862 was chosen solely for the purpose of illustration. **B**, Average jackknife correlation between 7A-to-V1
863 beta GC and V1-to-V4 gamma GC, averaged over triplets, then over monkeys. The solid black circle
864 shows the result for standard triplets, that is, triplets where the 7A-to-V1 beta GC and the V1-to-V4
865 gamma GC are connected through the same V1 site. As the distance between V1 sites increases,
866 there is a monotonic falloff in the correlation coefficient. The mean distance between V1 sites is color-
867 coded as solid circles matching the mean distances of the five distance intervals shown in **A**. The error
868 region shows ± 1 SEM across triplets per monkey, then averaged over monkeys.

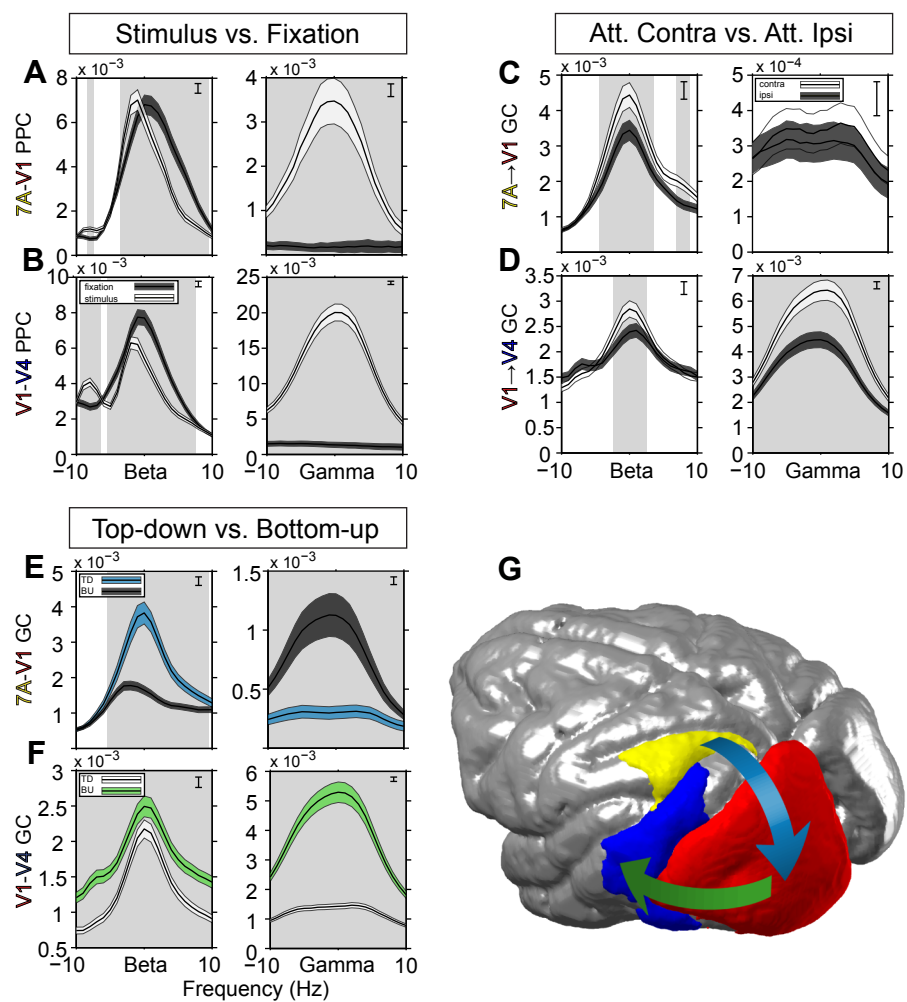
869 **Figure 8.** Lagged jackknife correlation (LJC) analysis. **A**, The solid red curve shows the LJC between
870 7A-to-V1 beta GC and V1-to-V4 gamma GC, averaged over triplets, then over monkeys. The blue
871 dashed line denotes the significance threshold ($p=0.05$, two-tailed non-parametric randomization test,
872 corrected for multiple comparisons across lags). The green vertical line indicates the lag of the
873 maximum LJC value, with ± 1 SEM indicated in red. The lag of the peak LJC value was significantly
874 different from zero ($t(10663) = -7.576$, $p < 0.001$, two-tailed). Solid gray curve: LJC between 7A-to-V1
875 gamma GC and V1-to-V4 beta GC, averaged over triplets, then over monkeys, which showed no
876 significant peaks.



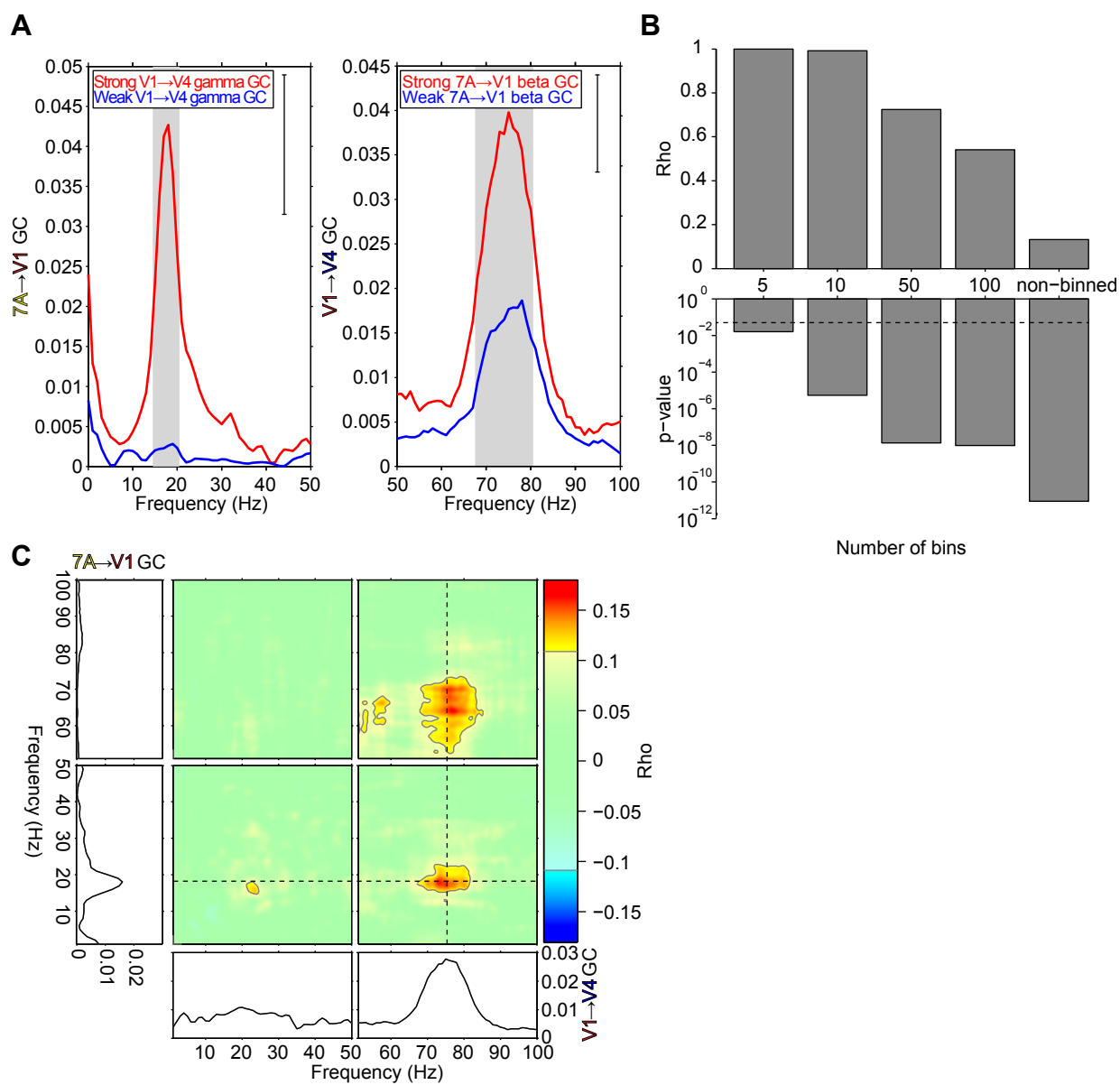
Richter et al., Fig. 1



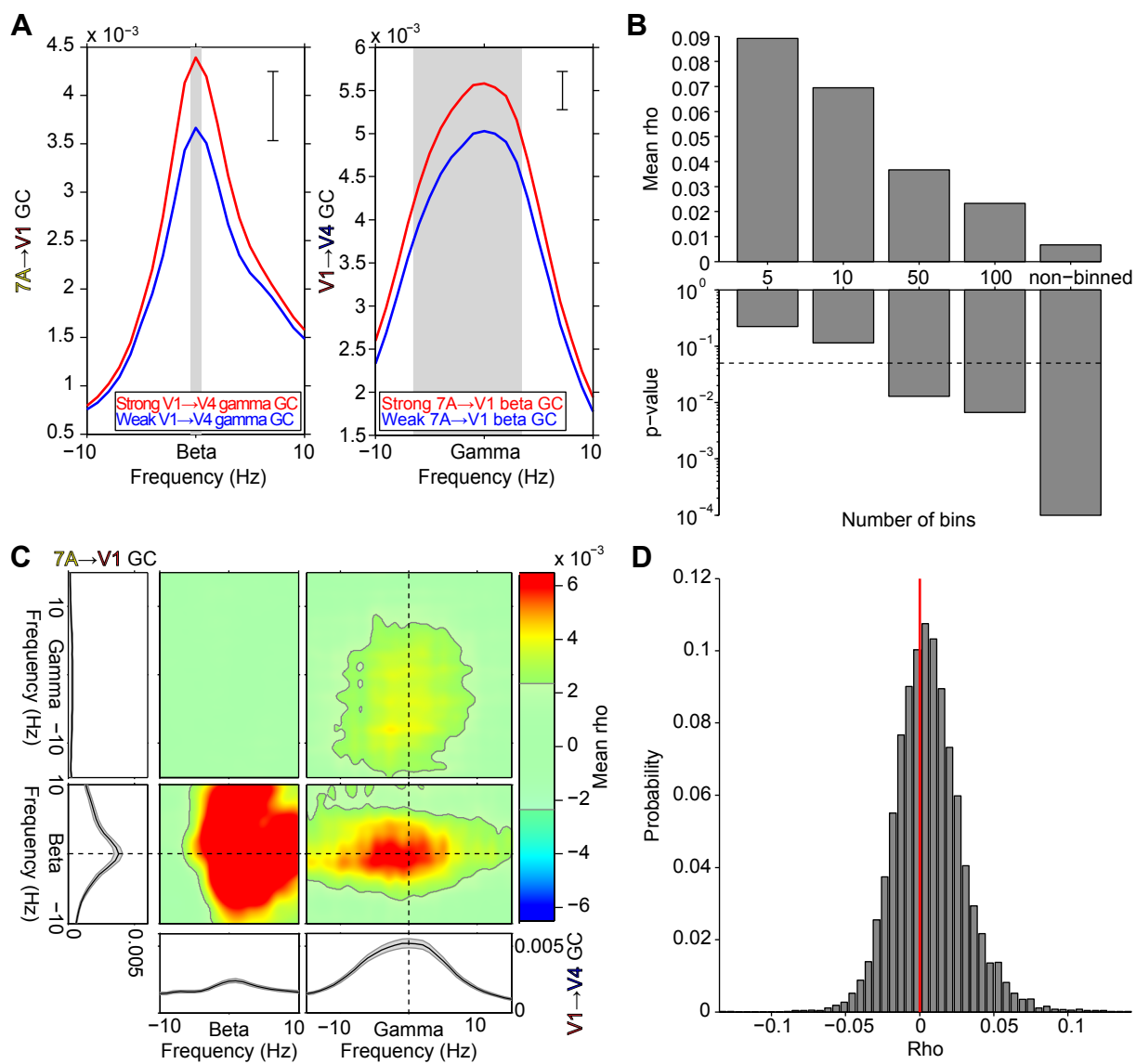
Richter et al., Fig. 2



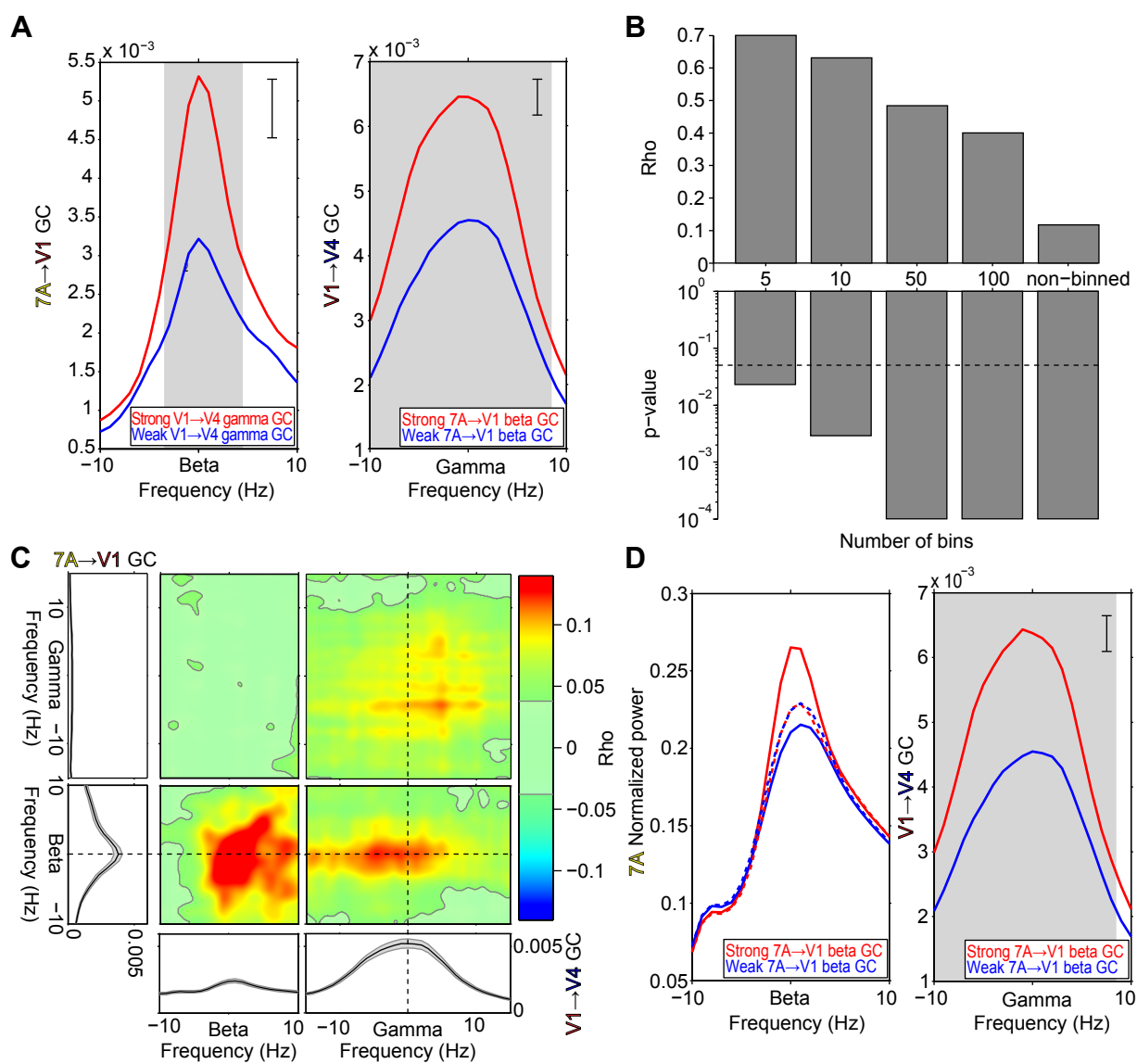
Richter et al., Fig. 3



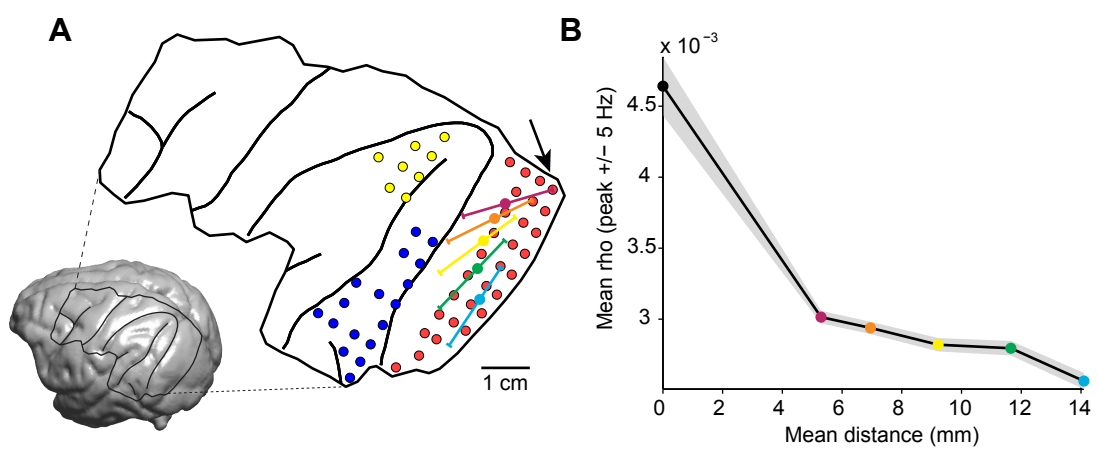
Richter et al., Fig. 4



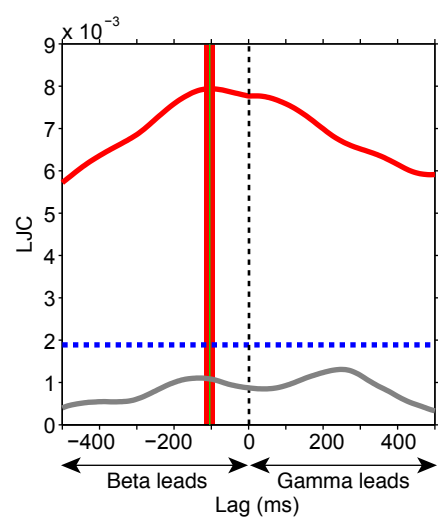
Richter et al., Fig. 5



Richter et al., Fig. 6



Richter et al., Fig. 7



Richter et al., Fig. 8